Gravitational-Wave Limits from Pulsar Timing Constrain Supermassive Black Hole Evolution

R. M. Shannon *et al.*

Science **342**, 334 (2013);
DOI: 10.1126/science.1238012

Science (print ISSN 0036-8075; online ISSN 1095-9203) is published weekly, except the last week in December, by the American Association for the Advancement of Science, 1200 New York Avenue NW, Washington, DC 20005.

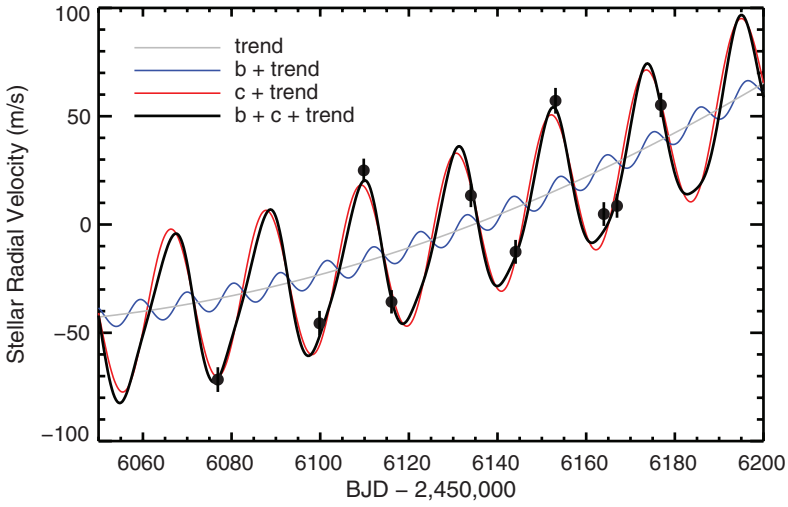

Fig. 3. Radial velocity variations. Solid circles show the individual radial velocity measurements as a function of barycentric Julian date (BJD).; the black solid line is the best-fitting photodynamical model to the combined Kepler and radial velocity data. Thin gray, blue, and red lines show the individual components of the fit, which includes a radial velocity drift modeled as a quadratic function of time and radial velocity variations due to planets b and c. The drift is attributed to a third, massive companion in a wide orbit.

period < 10 days) show a wide range of obliquities (*22*–*25*). This finding has been interpreted as supporting evidence for dynamical perturbations as the origin of hot Jupiters, and against scenarios in which hot Jupiters migrate inward because of an interaction with the protoplanetary disk (*26*). This conclusion, however, relies on the assumption that the stellar equator is a good tracer of the initial orbital plane of the planet (and hence the protoplanetary disk), which has previously been called into question (*27*, *28*). Important test cases are coplanar multiplanet systems, which, if primordial alignments are common, should predominantly show low obliquities. Indeed, until now all transiting multiplanet systems have been found to be well-aligned (*29*–*31*).

Although our observations do not constrain the primordial inclination of the protoplanetary disk of Kepler-56, they provide firm evidence that stellar spin-orbit misalignments are not solely confined to hot-Jupiter systems. Continued radial velocity measurements will reveal whether the third companion in the Kepler-56 system is a planet (implying that the initial misalignment occurred after the planets formed) or a star (implying a primordial misalignment of the protoplanetary disk).

References and Notes

1. W. J. Borucki *et al.*, *Science* **327**, 977–980 (2010).
2. N. M. Batalha *et al.*, *Astrophys. J.* **713**, L109–L114 (2010).
3. W. J. Borucki *et al.*, *Astrophys. J.* **736**, 19 (2011).
4. J. H. Steffen *et al.*, *Mon. Not. R. Astron. Soc.* **428**, 1077–1087 (2013).
5. J. De Ridder *et al.*, *Nature* **459**, 398–400 (2009).
6. See supplementary materials on *Science* Online.
7. W. A. Dziembowski, D. O. Gough, G. Houdek, R. Sienkiewicz, *Mon. Not. R. Astron. Soc.* **328**, 601–610 (2001).
8. J. Montalbán, A. Miglio, A. Noels, R. Scuflaire, P. Ventura, *Astrophys. J.* **721**, L182–L188 (2010).
9. P. G. Beck *et al.*, *Science* **332**, 205 (2011).
10. T. R. Bedding *et al.*, *Nature* **471**, 608–611 (2011).
11. L. Gizon, S. K. Solanki, *Astrophys. J.* **589**, 1009–1019 (2003).
12. P. G. Beck *et al.*, *Nature* **481**, 55–57 (2011).
13. D. Fabrycky, S. Tremaine, *Astrophys. J.* **669**, 1298–1315 (2007).
14. M. Nagasawa, S. Ida, T. Bessho, *Astrophys. J.* **678**, 498–508 (2008).
15. D. Lai, F. Foucart, D. N. C. Lin, *Mon. Not. R. Astron. Soc.* **412**, 2790–2798 (2011).
16. T. M. Rogers, D. N. C. Lin, H. H. B. Lau, *Astrophys. J.* **758**, L6 (2012).
17. M. R. Bate, G. Lodato, J. E. Pringle, *Mon. Not. R. Astron. Soc.* **401**, 1505–1513 (2010).
18. R. A. Mardling, *Mon. Not. R. Astron. Soc.* **407**, 1048–1069 (2010).
19. K. Batygin, *Nature* **491**, 418–420 (2012).
20. D. Queloz *et al.*, *Astron. Astrophys.* **359**, L13 (2000).
21. J. N. Winn *et al.*, *Astrophys. J.* **631**, 1215–1226 (2005).
22. J. A. Johnson *et al.*, *Proc. Astron. Soc. Pac.* **121**, 1104–1111 (2009).
23. J. N. Winn, D. Fabrycky, S. Albrecht, J. A. Johnson, *Astrophys. J.* **718**, L145–L149 (2010).
24. A. H. M. J. Triaud *et al.*, *Astron. Astrophys.* **524**, A25 (2010).
25. S. Albrecht *et al.*, *Astrophys. J.* **757**, 18 (2012).
26. D. N. C. Lin, P. Bodenheimer, D. C. Richardson, *Nature* **380**, 606–607 (1996).
27. J.-B. Le Bouquin *et al.*, *Astron. Astrophys.* **498**, L41–L44 (2009).
28. C. A. Watson *et al.*, *Mon. Not. R. Astron. Soc.* **413**, L71–L75 (2011).
29. T. Hirano *et al.*, *Astrophys. J.* **759**, L36 (2012).
30. R. Sanchis-Ojeda *et al.*, *Nature* **487**, 449–453 (2012).
31. W. J. Chaplin *et al.*, *Astrophys. J.* **766**, 101 (2013).

Acknowledgments: We gratefully acknowledge the entire Kepler team for making this paper possible. Funding for the Kepler Mission is provided by NASA's Science Mission Directorate. We thank E. Agol and D. Raggozine for helpful comments on the manuscript. Supported by an appointment to the NASA Postdoctoral Program at Ames Research Center, administered by Oak Ridge Associated Universities through a contract with NASA (D.H.); a NSF Graduate Research Fellowship (K.M.D.); a NSF Graduate Research Fellowship under grant DGE1144469 (B.T.M.); the Netherlands Organisation for Scientific Research (S.H.); BELSPO for contract PRODEX COROT (J.M.); the NASA Kepler Participating Scientist program (R.S.-O., J.N.W., and E.B.F.); NSF grant AST-1105930 (S.B.); and the David and Lucile Packard and Alfred P. Sloan foundations (J.A.J.). J.A.C. is a Hubble Fellow of the Harvard-Smithsonian Center for Astrophysics. Funding for the Stellar Astrophysics Centre is provided by Danish National Research Foundation grant DNRF106. The research is supported by the ASTERISK (Asteroseismic Investigations with SONG and Kepler) project funded by the European Research Council (grant agreement 267864).

Supplementary Materials

www.sciencemag.org/content/342/6156/331/suppl/DC1
Materials and Methods
Figs. S1 to S24
Tables S1 to S6
References (*32*–*119*)

18 June 2013; accepted 4 September 2013
10.1126/science.1242066

Gravitational-Wave Limits from Pulsar Timing Constrain Supermassive Black Hole Evolution

R. M. Shannon,[1]*† V. Ravi,[1,2]*† W. A. Coles,[3] G. Hobbs,[1] M. J. Keith,[1] R. N. Manchester,[1] J. S. B. Wyithe,[2] M. Bailes,[4] N. D. R. Bhat,[4,5] S. Burke-Spolaor,[6] J. Khoo,[1,7] Y. Levin,[8] S. Osłowski,[4] J. M. Sarkissian,[9] W. van Straten,[4] J. P. W. Verbiest,[10] J.-B. Wang[1,11]

The formation and growth processes of supermassive black holes (SMBHs) are not well constrained. SMBH population models, however, provide specific predictions for the properties of the gravitational-wave background (GWB) from binary SMBHs in merging galaxies throughout the universe. Using observations from the Parkes Pulsar Timing Array, we constrain the fractional GWB energy density (Ω_{GW}) with 95% confidence to be $\Omega_{GW}(H_0/73 \text{ kilometers per second per megaparsec})^2 < 1.3 \times 10^{-9}$ (where H_0 is the Hubble constant) at a frequency of 2.8 nanohertz, which is approximately a factor of 6 more stringent than previous limits. We compare our limit to models of the SMBH population and find inconsistencies at confidence levels between 46 and 91%. For example, the standard galaxy formation model implemented in the Millennium Simulation Project is inconsistent with our limit with 50% probability.

Supermassive black holes (SMBHs), with masses between 10^6 and 10^{11} solar masses, are observed to exist at the centers of all massive galaxies in the nearby universe and to have masses that scale closely with properties of their hosts (*1*, *2*). Together, these phenomena

suggest that the growth processes of SMBHs and of their host galaxies are connected. Galaxies, and groups of galaxies, are embedded in even larger dark matter halos, which form and evolve through the hierarchical merging of smaller dark matter halos and galaxies (*3*, *4*). Galaxy mergers are expected to result in binary SMBHs (*5*, *6*), which, though notoriously difficult to observe via electromagnetic signatures, are expected to be the strongest sources of gravitational waves in the universe (*7*). The universality of galaxy mergers implies the existence of a gravitational-wave background (GWB) from binary SMBHs (*8*, *9*).

The GWB is manifested as a red-noise process in pulse arrival time measurements from pulsars (*10*). Pulsar timing array groups search for evidence of the GWB in radio-frequency observations of millisecond pulsars, which have rivaled the stability of the best clocks on Earth over time scales of tens of years (*11*). The GWB is commonly parameterized by its wave amplitude spectrum, $h_c(f) = A(f/f_{yr})^{-2/3}$, where f is the received gravitational-wave frequency, f_{yr} is a reference frequency of one cycle per year, and A is the characteristic amplitude that defines the strength of the GWB. The fraction of the critical energy density of the universe, per logarithmic frequency interval (Ω_{GW}), of the GWB is $\Omega_{GW}(f) = (2\pi^2/3H_0^2)A^2 f_{yr}^2 (f/f_{yr})^{2/3}$ (*10*), where H_0 is the Hubble constant, which we assume to be 73 km s^{-1} Mpc^{-1}. Recent observations by two separate pulsar timing array groups have been analyzed to find $A < 6 \times 10^{-15}$ (*12*) and $< 7 \times 10^{-15}$ (*13*) with 95% confidence.

We have been monitoring pulse arrival times from 20 millisecond pulsars with the 64-m Parkes Telescope as part of the Parkes Pulsar Timing Array (PPTA) project (*14*) and previous observing programs (*15*). We extended the timing baseline of this data set by including publicly available observations from the Arecibo observatory (*16*). A detection of the GWB relies on measuring correlations between residual pulse arrival times for multiple pulsars with different angular separations on the sky. Within the PPTA timing program, there are presently too few pulsars with sufficient timing precision and data span to make an unambiguous detection of the GWB feasible (*17*). We instead use observations of six pulsars with the lowest noise levels over the longest observing spans to constrain the GWB amplitude (*18*) (Fig. 1).

Our limit on the strength of the GWB was computed in two stages (*19*). For each pulsar j, we first estimated the power spectral density $P_j(f_i)$ of the residual pulse arrival times after a fit for a pulsar model (*20*) at frequencies f_i that are harmonics of $1/T_{obs}$, where T_{obs} is the observing span for the pulsar. A prewhitening method (*21*) was used in the spectral estimation to eliminate spectral leakage and to provide nearly independent spectral estimates, even if red-noise signals, such as those expected from the GWB, are present. We form a detection statistic (DS) from the power spectra

$$\hat{A}^2 = \sum_{ij}[P_j(f_i)g_j(f_i)/M_j(f_i)^2]/\sum_{ij}[g_j(f_i)/M_j(f_i)]^2 \quad (1)$$

where $g_j(f_i)$ is the shape of the power spectrum induced by the GWB and $M_j(f_i)$ is a model of the observed spectrum (Fig. 1). The DS $\hat{A}^2$ combines individual spectral estimates $P_j(f_i)$ to form a conservative estimate of the square of the characteristic amplitude of the GWB (A^2). If the spectral models are correct, a DS of the form in Eq. 1 provides an estimate of A^2 with a maximal signal-to-noise ratio. To set a limit on A, we compared the observed value of the DS with distributions of the

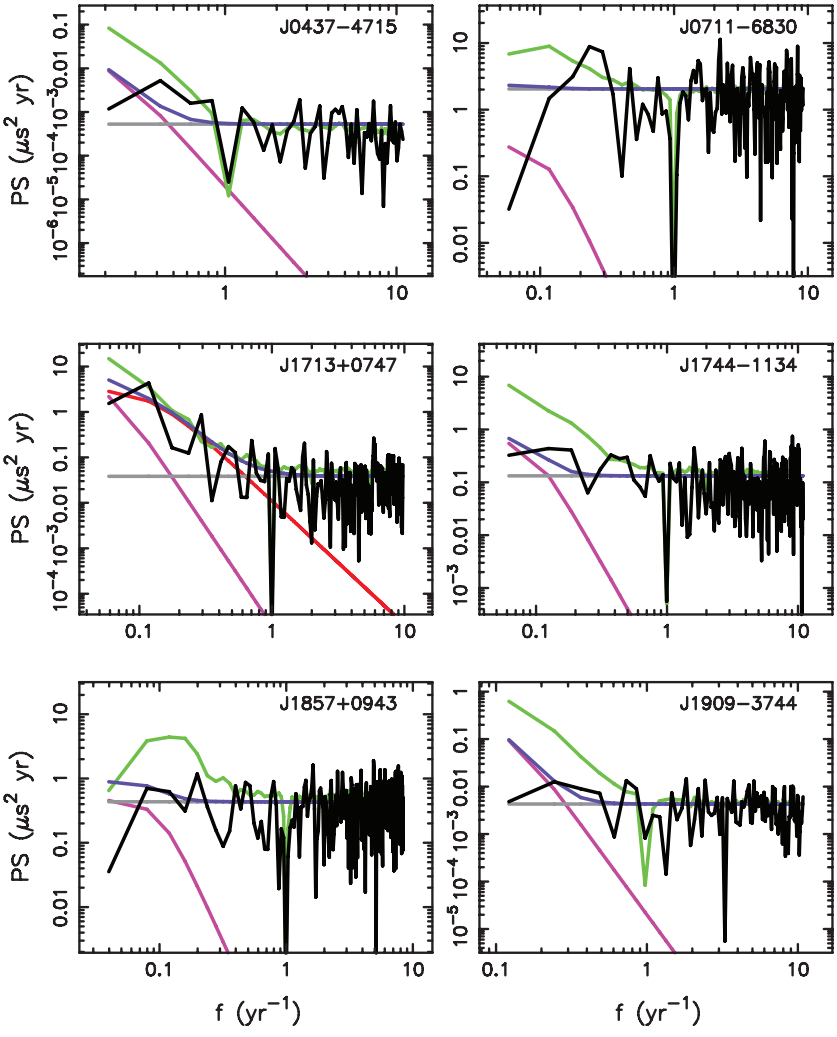

Fig. 1. Observed power spectra of the residual postfit arrival times and models of these spectra for the PPTA pulsars used to set the limit on the GWB amplitude. The observed power spectra (PS), P_j, for the pulsars are shown as black lines, along with the models of the PS, $M_j = W_j + G_j + R_j$ (shown as purple lines). The models contain a white component (W_j, gray lines), a common GWB component G_j (pink lines), and, for PSR J1713+0747, an additional red-noise term R_j (red line). The PS models were used only for the determination of the weights in the calculation of the detection statistic. The green curves show what the PS would look like (on average) in the presence of a Gaussian GWB with amplitude 2.4×10^{-15}. The names of the pulsars are given in the top-right corners of each panel.

[1]Commonwealth Scientific and Industrial Research Organisation (CSIRO) Astronomy and Space Science, Australia Telescope National Facility, Post Office Box 76, Epping, New South Wales 1710, Australia. [2]School of Physics, University of Melbourne, Parkville, Victoria 3010, Australia. [3]Department of Electrical and Computer Engineering, University of California at San Diego, La Jolla, CA 92093, USA. [4]Centre for Astrophysics and Supercomputing, Swinburne University of Technology, Post Office Box 218, Hawthorn, Victoria 3122, Australia. [5]International Centre for Radio Astronomy Research, Curtin University, Bentley, Western Australia 6102, Australia. [6]Jet Propulsion Laboratory, California Institute of Technology, 4800 Oak Grove Drive, Pasadena, CA 91109–8099, USA. [7]CSIRO Advanced Scientific Computing, Information Management and Technology, Private Bag 33, Clayton, Victoria 3169, Australia. [8]School of Physics, Monash University, Post Office Box 27, Victoria 3800, Australia. [9]CSIRO Astronomy and Space Science, Parkes Observatory, Post Office Box 276, Parkes, New South Wales 2870, Australia. [10]Max-Planck-Institut für Radioastronomie, Auf dem Hügel 69, 53121 Bonn, Germany. [11]Xinjiang Astronomical Observatory, Chinese Academy of Sciences, 150 Science 1-Street, Urumqi, Xinjiang 830011, China.

*Corresponding author. E-mail: ryan.shannon@csiro.au (R.M.S.); v.ravi@pgrad.unimelb.edu.au (V.R.)
†These authors contributed equally to this work.

DS derived from simulated data sets, which include white noise consistent with the observations and a GWB of strength A_{sim}. Many trial simulations were conducted at a given A_{sim} to account for the stochasticity of the GWB. The 95% confidence limit on the GWB amplitude, A_{95}, is the value of A_{sim} at which only 5% of the $\hat{A}^2$ trials are lower than the observed $\hat{A}^2$.

We simulated both Gaussian (*10*) and non-Gaussian (*9*) GWB-induced residual pulse arrival times. Although previous pulsar timing array limits on the strength of the GWB (*12*, *13*) were derived assuming Gaussian statistics, a non-Gaussian background, dominated by fewer binary SMBHs, is predicted from some models of the binary SMBH population (*8*, *9*).

We verified the efficacy of the algorithm by correctly bounding the GWB strength in synthetic data sets, including those in the International Pulsar Timing Array Data Challenge and other mock data sets that contained features of the observations such as inhomogeneous observing cadence, highly heteroscedastic pulse arrival times, and red noise (*22*). When applied to the PPTA data set, and assuming a Gaussian GWB, we find that $\Omega_{GW}(f_{PPTA})(H_0/73\ km\ s^{-1}\ Mpc^{-1})^2 < 1.3 \times 10^{-9}$ with 95% confidence at a gravitational-wave frequency (f_{PPTA}) of 2.8 nHz (*23*). This is equivalent to $A_{95} = 2.4 \times 10^{-15}$. Compared with the power spectra P_j of the measured residual pulse arrival times, the mean power spectra of 200 simulated realizations with $A_{sim} = A_{95}$ (displayed in Fig. 1 as green lines) show, as expected, excess power at the lowest frequencies. For a non-Gaussian GWB, we find $\Omega_{GW}(f_{PPTA})(H_0/73\ km\ s^{-1}\ Mpc^{-1})^2 < 1.6 \times 10^{-9}$ with 95% confidence, corresponding to $A_{95} = 2.7 \times 10^{-15}$.

The PPTA bound on the GWB enables direct tests of models for galaxy and SMBH formation that specify the population of binary SMBHs in the universe. We compared the probability $Pr(\Omega_{GW})$ that a GWB of energy density $\Omega_{GW}(f_{PPTA})$ exists, given the PPTA observations with four predictions for the GWB from binary SMBHs, expressed as the probability density function of $\Omega_{GW}(f_{PPTA})$, $\rho_M(\Omega_{GW})$ (*24*) (Fig. 2). All four predictions account for the most recent SMBH mass and galaxy bulge mass measurements and include the assumption that all binary SMBHs that contribute to the GWB are in circular orbits and not interacting with their environments.

First, a model that assumes a scenario in which all evolution in the galaxy stellar mass function and in the SMBH mass function is merger-driven at redshifts $z < 1$ (*25*) predicts a Gaussian GWB that is ruled out at the 91% confidence level. However, the assumption of purely merger-driven evolution leads to the largest possible GWB amplitude, given observational data.

A synthesis of possible combinations of current observational estimates of the galaxy merger rate and SMBH-galaxy scaling relations results in a large range of possible GWB amplitudes (*26*). PPTA observations exclude 46% of this set of GWB amplitudes, assuming a Gaussian GWB.

As a specific example for how pulsar timing array observations can affect models of SMBH formation and growth, we calculated the level of $\Omega_{GW}(f_{PPTA})$ (*24*) expected from a semi-analytic galaxy formation model (*4*) implemented within the Millennium (*27*) and Millennium-II (*28*) dark matter simulations. This model, in which SMBHs are seeded in every galaxy merger remnant at early times and grow primarily by gas accretion triggered by galaxy mergers, represents the standard paradigm of galaxy and SMBH formation and evolution. The model accurately reproduces the luminosity function of quasars at $z < 1$ corresponding to the epoch predicted to dominate the GWB (*8*, *25*, *26*). The range of predictions for $\Omega_{GW}(f_{PPTA})$ results from the finite observational sample of measured SMBH and bulge mass pairs (*2*), which is used to tune the model, but neither accounts for uncertainties in the observed galaxy stellar mass function (*4*) nor in the nature of the relations between SMBH masses and bulge masses (*2*). Assuming a non-Gaussian GWB, the probability that this prediction for $\rho_M(\Omega_{GW})$ will be inconsistent with the PPTA data is 49%.

A complementary prediction for the strength of the GWB comes from an independent model for SMBH growth at late times (*29*). This model examines the growth mechanisms of SMBHs in cluster and void environments through mergers and gas accretion. The model is inconsistent with the PPTA data at the 61% confidence level.

The PPTA constraints on the GWB show that pulsar timing array observations have reached a sufficient level of sensitivity to test models for the binary SMBH population. The highest galaxy merger rate that is consistent with the observed evolution in the galaxy stellar mass function (*25*) is inconsistent with our limit. We exclude 46% of the parameter space of a model that surveys empirical uncertainties in the growth and merger of galaxies and black holes (*26*); therefore, our results reduce these uncertainties. Although the PPTA limit excludes only 49 and 61% of realizations of the GWB from two galaxy and SMBH evolution models, these models are open to refinement. For example, these models do not include SMBH formation mechanisms consistent with high-redshift quasar observations (*30*), nor do

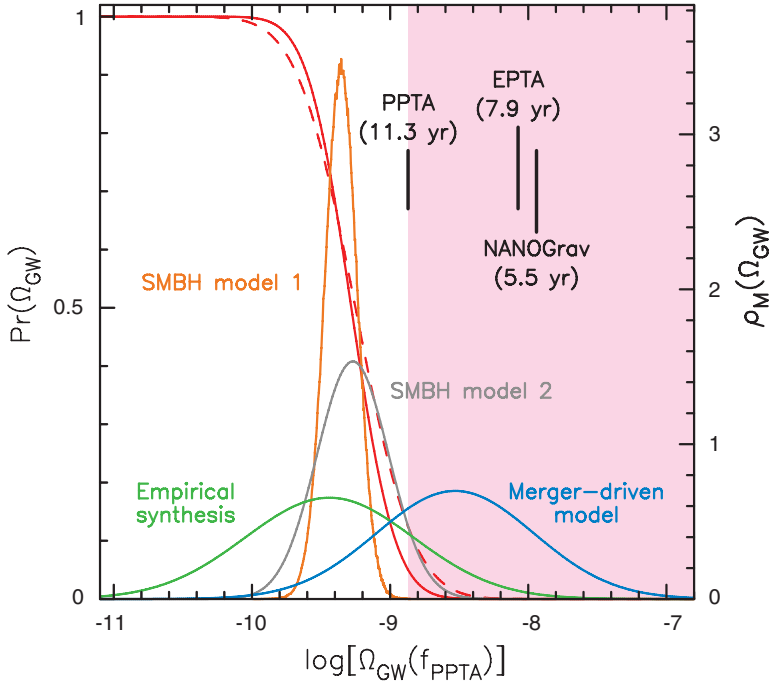

Fig. 2. Comparison between the PPTA constraints on $\Omega_{GW}(f_{PPTA})$ and various model predictions (*24*). Given the PPTA data, the probabilities $Pr(\Omega_{GW})$ that a GWB relative energy density $\Omega_{GW}(f_{PPTA})$ exists, assuming Gaussian (*10*) and non-Gaussian (*9*) GWB statistics, are shown as red solid and dashed lines, respectively. The pink shaded area represents the values of $\Omega_{GW}(f_{PPTA})$ ruled out with greater than 95% confidence, assuming a Gaussian GWB. The labeled curves represent the probability density functions $\rho_M(\Omega_{GW})$ for $\Omega_{GW}(f_{PPTA})$ predicted by a synthesis of empirical models (*26*) (green), assuming merger-driven galaxy evolution at redshifts $z < 1$ (*25*) (blue), from the semi-analytic galaxy formation model (SMBH model 1, orange) that we discuss in the text and from a second distinct model (*29*) for SMBH growth (SMBH model 2, gray). When integrated over Ω_{GW}, the product of $Pr(\Omega_{GW})$ and $\rho_M(\Omega_{GW})$ gives the probability of the model being consistent with the data. The vertical bars indicate the 95% confidence upper limits on $\Omega_{GW}(f_{PPTA})$, assuming a Gaussian GWB from the PPTA, and recently published limits from the European Pulsar Timing Array (EPTA) (*12*) and the North American Nanohertz Observatory for Gravitational Waves (NANOGrav) (*13*) scaled to f_{PPTA}. The times next to the limits correspond to the reciprocal of the frequency of maximum sensitivity and are approximately the observing span of the data sets (*12*, *13*, *23*).

they reproduce the observed larger scatter and possibly higher normalization in SMBH-galaxy scaling relations for the most massive SMBHs (*1*, *2*). Other physical effects will also be built into the next generation of GWB models. For example, recent numerical simulations of massive galaxy mergers predict binary SMBHs with eccentricities ranging between 0.1 (*31*) and 0.9 (*32*). If binaries radiating gravitational waves at frequencies relevant to pulsar timing arrays are considerably eccentric or predominantly evolving under environmental interactions (*33*), the spectral shape of $\Omega_{GW}(f)$ may differ from current predictions (*34*).

References and Notes

1. J. Kormendy, L. Ho, *Annu. Rev. Astron. Astrophys.* **51**, 511–653 (2013).
2. N. J. McConnell, C.-P. Ma, *Astrophys. J.* **764**, 184 (2013).
3. D. J. Croton *et al.*, *Mon. Not. R. Astron. Soc.* **365**, 11–28 (2006).
4. Q. Guo *et al.*, *Mon. Not. R. Astron. Soc.* **413**, 101–131 (2011).
5. M. C. Begelman, R. D. Blandford, M. J. Rees, *Nature* **287**, 307–309 (1980).
6. M. Volonteri, F. Haardt, P. Madau, *Astrophys. J.* **582**, 559–573 (2003).
7. B. S. Sathyaprakash, B. F. Schutz, *Living Rev. Relativ.* **12**, 2 (2009).
8. A. Sesana, A. Vecchio, C. N. Colacino, *Mon. Not. R. Astron. Soc.* **390**, 192–209 (2008).
9. V. Ravi *et al.*, *Astrophys. J.* **761**, 84 (2012).
10. G. B. Hobbs *et al.*, *Mon. Not. R. Astron. Soc.* **394**, 1945–1955 (2009).
11. R. S. Foster, D. C. Backer, *Astrophys. J.* **361**, 300–308 (1990).
12. R. van Haasteren *et al.*, *Mon. Not. R. Astron. Soc.* **414**, 3117–3128 (2011).
13. P. B. Demorest *et al.*, *Astrophys. J.* **762**, 94 (2013).
14. R. N. Manchester *et al.*, *Publ. Astron. Soc. Aust.* **30**, e017 (2013).
15. J. P. W. Verbiest *et al.*, *Mon. Not. R. Astron. Soc.* **400**, 951–968 (2009).
16. V. M. Kaspi, J. H. Taylor, M. F. Ryba, *Astrophys. J.* **428**, 713–728 (1994).
17. D. R. B. Yardley *et al.*, *Mon. Not. R. Astron. Soc.* **414**, 1777–1787 (2011).
18. The data sets are described in supplementary text section S1.
19. Additional description of the algorithm is found in supplementary text section S2.
20. R. Edwards, G. B. Hobbs, R. N. Manchester, *Mon. Not. R. Astron. Soc.* **372**, 1549–1574 (2006).
21. W. Coles, G. Hobbs, D. J. Champion, R. N. Manchester, J. P. W. Verbiest, *Mon. Not. R. Astron. Soc.* **418**, 561–570 (2011).
22. Details of the data challenge and other tests can be found in supplementary text section S2 and table S2.
23. The algorithm used for calculating f_{PPTA} is described in supplementary text section S3.
24. Corrections to previous models for the GWB are outlined in supplementary text section S4. The models for the GWB are described in additional detail in supplementary text sections S5 and S6. The probabilities used to compare these models to the PPTA limit are calculated in supplementary text section S7.
25. S. T. McWilliams, J. P. Ostriker, F. Pretorius, http://arxiv.org/abs/1211.5377 (2012).
26. A. Sesana, *Mon. Not. R. Astron. Soc.* **433**, L1–L5 (2013).
27. V. Springel *et al.*, *Nature* **435**, 629–636 (2005).
28. M. Boylan-Kolchin, V. Springel, S. D. M. White, A. Jenkins, G. Lemson, *Mon. Not. R. Astron. Soc.* **398**, 1150–1164 (2009).
29. A. Kulier, J. P. Ostriker, P. Natarajan, C. N. Lackner, R. Cen, http://arxiv.org/abs/1307.3684 (2013).
30. Z. Haiman, *Astrophys. Space Sci. Library* **396**, 293–341 (2013).
31. F. M. Khan, K. Holley-Bockelmann, P. Berczik, A. Just, *Astrophys. J.* **773**, 100 (2013).
32. F. M. Khan *et al.*, *Astrophys. J.* **749**, 147 (2012).
33. C. Roedig, A. Sesana, *J. Phys. Conf. Ser.* **363**, 012035 (2012).
34. M. Enoki, M. Nagashima, *Prog. Theor. Phys.* **117**, 241–256 (2007).

Acknowledgments: We thank all of the observers, engineers, and Parkes observatory staff members who have assisted with the observations reported in this paper. We thank N. McConnell for providing and confirming some dynamical SMBH and bulge mass measurements, S. Mutch for discussions on the Millennium-based model, and X.-J. Zhu for comments on the manuscript. The Parkes radio telescope is part of the Australia Telescope National Facility, which is funded by the Commonwealth of Australia for operation as a National Facility managed by CSIRO. The Millennium and Millennium-II Simulation databases used in this paper and the Web application providing online access to these databases were constructed as part of the activities of the German Astrophysical Virtual Observatory. The PPTA project was initiated with support from R.N.M.'s Australian Research Council (ARC) Federation Fellowship (no. FF0348478) and from the CSIRO under that fellowship program. The PPTA project has also received support from ARC Discovery Project grant no. DP0985272. V.R. is a recipient of a John Stocker Postgraduate Scholarship from the Science and Industry Endowment Fund, G.H. is the recipient of an ARC QEII Fellowship (no. DP0878388), and J.S.B.W. acknowledges an Australian Research Council Laureate Fellowship. Part of this research was carried out at the Jet Propulsion Laboratory, California Institute of Technology, under a contract with NASA. J.P.W.V. acknowledges the financial support by the European Research Council (ERC) for the ERC Starting Grant Beacon under contract no. 279202. The authors declare no conflicts of interest. Data used in this analysis can be accessed via the Australia National Data Service (www.ands.org.au).

Supplementary Materials

www.sciencemag.org/content/342/6156/334/suppl/DC1
Supplementary Text
Fig. S1
Tables S1 and S2
References (*35*–*51*)

19 March 2013; accepted 6 September 2013
10.1126/science.1238012

Strain-Induced Ultrahard and Ultrastable Nanolaminated Structure in Nickel

X. C. Liu,[1]* H. W. Zhang,[1]* K. Lu[1,2]†

Heavy plastic deformation may refine grains of metals and make them very strong. But the strain-induced refinement saturates at large strains, forming three-dimensional ultrafine-grained (3D UFG) structures with random orientations. Further refinement of this microstructure is limited because of the enhanced mobility of grain boundaries. Very-high-rate shear deformation with high strain gradients was applied in the top surface layer of bulk nickel, where a 2D nanometer-scale laminated structure was induced. The strongly textured nanolaminated structure (average lamellar thickness of 20 nanometers) with low-angle boundaries among the lamellae is ultrahard and ultrastable: It exhibits a hardness of 6.4 gigapascal—which is higher than any reported hardness of the UFG nickel—and a coarsening temperature of 40 kelvin above that in UFG nickel.

Metals can be strengthened by introducing more grain boundaries (GBs) via grain refinement (*1*, *2*) or alternatively by generating more dislocations (*3*). Remarkable hardening in metals and alloys induced through heavy plastic deformation originates from both mechanisms: Grains are refined to the sub-micrometer or nanometer scales, and stored dislocation density is pumped up by orders of magnitude. However, as the strains exceed values between 5 and 30, saturation in grain refinement leads to steady-state three-dimensional (3D) ultrafine-grained (UFG, sub-micrometer–sized) structure with random orientations (*4*–*6*). Further increases in strain, however, can lead to grain coarsening and dislocation annihilation (*7*, *8*). As grain size drops into the submicro- or nanoscale, GB migration becomes so pronounced that grains coarsen even at ambient temperature (*9*). Because the dislocation multiplication from straining is balanced by the dislocation annihilation due to GB migration, strain-induced structural evolution ceases, and dislocation density reaches its limit, which in heavily deformed metals is typically $\sim 10^{15}$ m^{-2}.

Among various processing parameters of plastic deformation, strain rate, deformation temperature, and strain gradient seem most relevant to dislocation multiplication and, hence, to structure refinement or reduction of boundary spacing, which governs strength and other mechanical properties of materials. Deformation at high strain rates or at low temperatures may suppress dislocation annihilation kinetics and facilitate forming more GBs or dislocation boundaries. For instance, when nickel (Ni) is compressed at a rate

[1]Shenyang National Laboratory for Materials Science, Institute of Metal Research, Chinese Academy of Sciences, Shenyang 110016, China. [2]Herbert Gleiter Institute of Nanoscience, Nanjing University of Science and Technology, Nanjing 210094, China.

*These authors contributed equally to this work.
†Corresponding author. E-mail: lu@imr.ac.cn